

ODD-SEC: Onboard Drone Detection with a Spinning Event Camera

Kuan Dai*, Hongxin Zhang*, Sheng Zhong, Yi Zhou

Abstract—The rapid proliferation of drones requires balancing innovation with regulation. To address security and privacy concerns, techniques for drone detection have attracted significant attention. Passive solutions, such as frame camera-based systems, offer versatility and energy efficiency under typical conditions but are fundamentally constrained by their operational principles in scenarios involving fast-moving targets or adverse illumination. Inspired by biological vision, event cameras asynchronously detect per-pixel brightness changes, offering high dynamic range and microsecond-level responsiveness that make them uniquely suited for drone detection in conditions beyond the reach of conventional frame-based cameras. However, the design of most existing event-based solutions assumes a static camera, greatly limiting their applicability to moving carriers—such as quadrupedal robots or unmanned ground vehicles—during field operations. In this paper, we introduce a real-time drone detection system designed for deployment on moving carriers. The system utilizes a spinning event-based camera, providing a 360° horizontal field of view and enabling bearing estimation of detected drones. A key contribution is a novel image-like event representation that operates without motion compensation, coupled with a lightweight neural network architecture for efficient spatiotemporal learning. Implemented on an onboard Jetson Orin NX, the system can operate in real time. Outdoor experimental results validate reliable detection with a mean angular error below 2° under challenging conditions, underscoring its suitability for real-world surveillance applications. We will open-source our complete pipeline to support future research.

I. INTRODUCTION

Drones are increasingly adopted in fields such as aerial photography, precision agriculture, logistics, search and rescue, and environmental monitoring [1]–[3], owing to their low cost and versatility. However, improper or malicious use poses risks to safety, security, privacy, and airspace operations [4]. Addressing these issues is therefore crucial to ensure the safe and beneficial integration of drones into society.

Inspired by the human visual system, event-based cameras asynchronously report per-pixel brightness changes [5], providing rich motion information, high dynamic range (HDR), and fine-grained temporal cues embedded in the event stream. Zhou *et al.* [6] leverage these unique characteristics to accurately identify independently moving objects from the fine-grained asynchronous event stream, while Wang

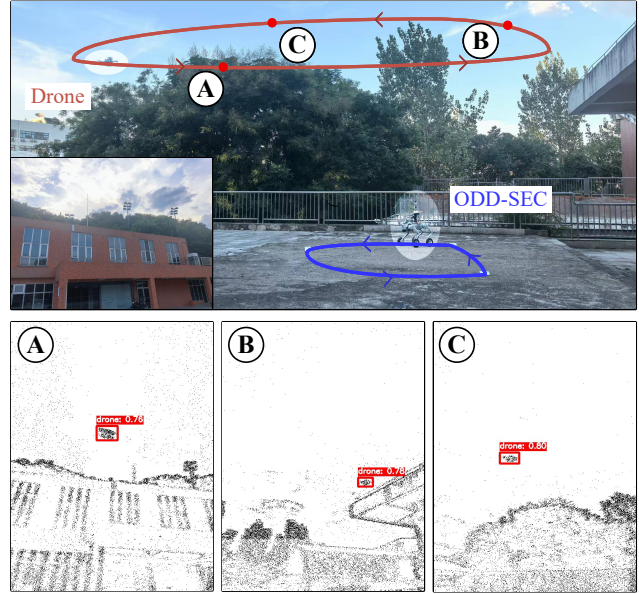


Fig. 1: Illustration of our system operating in an outdoor scenario. Top: The scene with the trajectories of the drone (in red) and our device (in blue), with an inset at the bottom-left showing the rear view of the same scene. Bottom: The detection results from our system. Specific measurement locations are marked with circled letters.

et al. [7] propose AEB Tracker, achieving over 50 kHz update rates under challenging illumination. However, the inherently limited field of view (FoV) of event cameras restricts their detection range, as the unpredictable flight trajectories of drones can easily cause them to leave the camera’s observable range, resulting in detection failure.

A recent effort to address this limitation is the SFERA system proposed by Da *et al.* [8], which employs back-to-back event cameras to achieve full 360° omnidirectional coverage, enabling drone detection and angular localization relative to the device. This approach, however, implicitly assumes a static viewpoint, as all validation is conducted on a tripod-mounted system. Such a design is insufficient for dynamic deployment scenarios such as on moving carriers, where unaddressed ego-motion could compound known system instabilities, e.g., tracker failures requiring re-initialization, and corrupt the entire perceptual pipeline.

To overcome these challenges, we propose ODD-SEC: an onboard system that integrates a spinning event camera, a spinning module, and an edge computer for real-time drone detection. The spinning camera enables omnidirec-

All authors are with the Neuromorphic Automation and Intelligence Lab (NAIL) at School of Artificial Intelligence and Robotics, Hunan University, Changsha, China.

* denotes equal contribution.

Corresponding author: Yi Zhou. Email: eeyzhou@hnu.edu.cn.

This work was supported by the National Key Research and Development Project of China under Grant 2023YFB4706600.

tional drone detection with panoramic horizontal coverage, overcoming FoV limitations and supporting long-term tracking. We integrate all modules into a self-contained system capable of deployment on moving carriers, such as a quadruped robot, for effective drone detection, as shown in Fig. 1. The core contributions of this paper are as follows:

- A novel event-based drone detection system design enabling 360° panoramic perception via a platform-mounted spinning event camera. This design effectively expands the FoV, overcoming the inherent FoV limitations of traditional event camera setups.
- A temporally-aware variant of the YOLOX network, taking a specific image-like representation of events as input, effectively addresses the challenges of massive data volume and motion blur caused by camera ego-motion and carrier movement.
- A comprehensive outdoor experiment conducted on a moving carrier validates the system’s capability to achieve reliable detection performance. The system achieves real-time drone detection and bearing estimation on Jetson Orin NX, demonstrating practical deployment capability. We will release our pipeline as an open-source code for future research in this field.

II. RELATED WORK

In line with the focus of our work, we review two closely related areas: event-camera-based object detection, which underpins our detection module, and FoV extension methods, which are essential to overcoming the inherent FoV limitations of event cameras.

A. Object Detection for Event Cameras

Event-based object detection methods can be broadly categorized into two paradigms according to their representation of events: point-based models and image-based models. The former paradigm leverages the sparse and asynchronous nature of event data, often employing spiking neural networks (SNNs) [9]–[11] or graph-based processing techniques [12, 13]. While effectively preserving the spatiotemporal distribution of raw events, these methods often face challenges related to data sparsity and computational efficiency. In contrast, the image-based models convert event streams into dense, frame-like representations, enabling the use of well-established convolutional neural networks. Some works in this line, such as [14]–[17], extract spatiotemporal features using stacked representations from consecutive short time windows. Although these approaches may not fully exploit the temporal information inherent in event streams, they have demonstrated competitive detection performance and remain dominant in practical applications.

Beyond these primary categories, several studies explore hybrid systems that combine event cameras with conventional frame-based sensors [18]–[20], leveraging complementary attributes of both modalities to enhance detection robustness. Furthermore, for specific moving objects such as drones, some researchers have analyzed the kinematic models of targets and achieved detection of specific objects

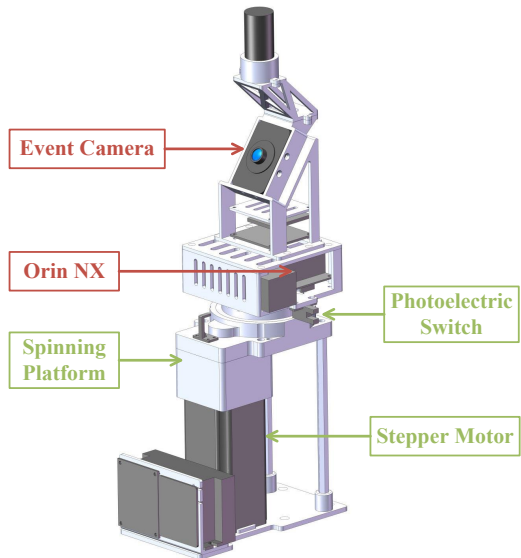


Fig. 2: CAD model of the system. Red and green boxes represent the actuation module and the perception-computing module, respectively.

by leveraging such models, without the need for training deep neural networks [21, 22].

B. FoV Extension Methods

The most straightforward approach to expanding a camera’s FoV is through specialized lenses, such as fisheye lenses [8, 23]. Another commonly used option is Panoramic Annular Lenses; for instance, the lens adopted in [24] provides a FoV of $360^\circ \times (40^\circ\text{--}120^\circ)$, directly enabling panoramic coverage. However, since the camera resolution remains unchanged, the resulting images tend to be more blurred.

An alternative strategy involves extending the FoV through camera motion. For example, visual servoing techniques [25, 26] enable active control of camera pose to dynamically expand the effective FoV, allowing the system to track targets and cover larger workspaces—though at the cost of increased system complexity due to perception–control coupling. A simpler motion-based approach is to employ continuous camera rotation. Schraml *et al.* [27] develop an event-driven stereo vision system using a pair of rotating single-column Dynamic Vision Sensors, achieving real-time 360° 3D panoramic reconstruction with high dynamic range performance.

III. METHODOLOGY

In this section, we detail the method of our system. We first introduce the hardware setup and mounting details of the proposed system (Sec. III-A). Then, we discuss the algorithms used in our system (Sec. III-B), including the drone detection network and positioning strategy.

A. Hardware Setup

The CAD model of our system hardware is shown in Fig. 2, with the specifications of the primary devices listed

TABLE I: Hardware setup and parameters.

Devices	Parameters
Event Camera (DVXplorer)	640×480 1/2.5" FoV: 77.32°× 61.93° 3.6-mm lens
Stepper Motor	Step angle: 1.8° Torque: 2.8 N·m Controller: TB6600
Spinning Platform	Reduction ratio: 5:1
Photoelectric Switch	Response time: <0.5 ms

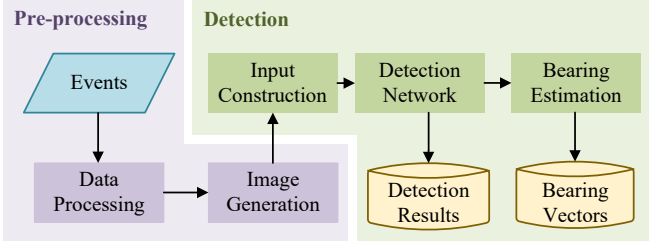


Fig. 3: Flowchart of the proposed algorithm. The two modules are executed independently. The Pre-processing part receives data from the event camera and converts it into image slices. The Detection part receives and processes the image stream, performs network inference, and calculates the relative bearing to the system based on the detection results.

in Tab. I. The hardware consists of two modules: an actuation module responsible for spinning the camera, and a perception-computing module dedicated to data recording and processing.

To achieve a 360° horizontal FoV, the actuation module spins the sensing-computing module via a stepper-motor-driven spinning platform. The motor is controlled by a battery-powered STM32-based driver for precise speed and direction regulation. During startup, the motor initially runs at a lower speed and then gradually accelerates to a constant angular velocity of 0.95 rad/s (to be distinguished from the Pulses Per Second (PPS) rate; detailed rationale in Sec. IV-A), thereby avoiding excessive acceleration that can lead to step loss. A photoelectric switch mounted on the spinning platform defines the zero-point direction. It is triggered once per rotation and provides a synchronization signal to the event camera, ensuring angular alignment and accurate orientation recovery.

The DVXplorer event camera serves as the primary sensor. To maximize coverage of potential drone flight areas, the camera is oriented vertically with a 35° upward tilt. The spinning platform’s rotation axis passes through the camera’s optical center. To address the potential high-bandwidth data transmission challenges caused by continuous rotation, the edge computing unit spins together with the camera assembly. This integrated computing unit directly receives raw

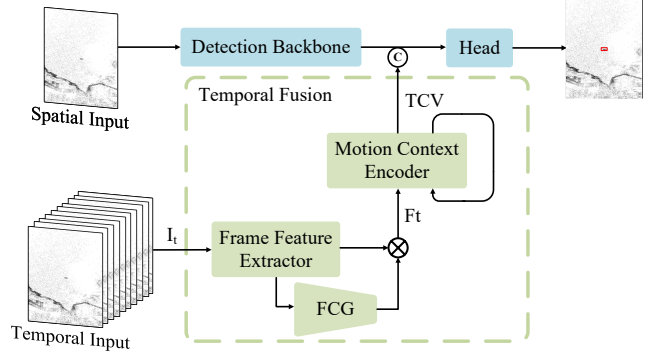


Fig. 4: Overview of the proposed detection network. Our novel Temporal Fusion Module (highlighted in a green dashed border) enhances detection by analyzing a sequence of frames that capture motion relationships. It employs Feature Channel Gating (FCG) to adaptively weight features, aggregates Temporal Context Vector (TCV) across the segment, and fuses it with features from the detection backbone to improve the network’s target recognition accuracy.

sensor data and executes the proposed algorithm, achieving end-to-end real-time drone detection without relying on slip rings or wireless transmission for high-bandwidth data.

All devices are battery-powered, enabling the system to operate independently. In addition, the actuation module is equipped with a mounting interface, facilitating integration with mobile carriers.

B. Algorithm Design

The proposed algorithm (shown in Fig. 3) takes in event data output by the spinning event camera, detects the 2D position of the drone, and calculates the bearing vector between the drone and our system. In the pre-processing module, raw events are transformed into a multi-slice spatio-temporal representation (MSR) to decouple target kinematics from rotation-induced spatial smearing (Sec. III-B.1). In the subsequent detection module, these slices are then processed by the Temporal Fusion Module (TFM), embedded within the YOLOX framework [28], to align robust features and adaptively suppress background noise (Sec. III-B.2). For precise localization under extreme target scale variations, we employ a scale-aware loss that explicitly decouples the penalty terms for central point distance and aspect ratio (Sec. III-B.3). Finally, the bearing estimation module translates these 2D detections into precise relative angles using camera intrinsics and real-time orientation data (Sec. III-B.4).

1) *Multi-slice Spatio-temporal Representation*: Conventional 2D event representations (e.g., Time Surface [29]) suffer from severe information loss during continuous rotation due to dense event overwriting. To preserve fine-grained temporal cues and mitigate rotation-induced spatial smearing, we construct a sequential representation by dividing a fixed temporal window ΔT into N uniform sub-intervals. The i -th spatio-temporal slice S_i is generated by:

$$S_i(x, y) = \sum_{e_k \in \Delta t_i} p_k \cdot \delta(x - x_k, y - y_k), \quad (1)$$

where $e_k = (x_k, y_k, t_k, p_k)$ represents an event triggered at timestamp t_k with polarity p_k at spatial coordinates (x_k, y_k) , $\Delta t_i = [T + \frac{i-1}{N}\Delta T, T + \frac{i}{N}\Delta T]$ is the i -th consecutive interval, and $\delta(\cdot)$ denotes the Dirac delta function. By partitioning the accumulation window into multiple slices, this representation effectively captures motion patterns while mitigating ego-motion-induced blur.

2) *Temporal Fusion Module*: Processing the generated slices as independent frames fails to capture the temporal evolution of the scene, limiting the network’s ability to utilize crucial motion cues. To capture the scene’s temporal evolution, we propose a dual-branch architecture, as illustrated in Fig. 4. The primary backbone extracts spatial features from the current slice, while TFM processes the entire MSR to encode motion context. While the primary backbone extracts spatial features from the current slice, MSR is processed by TFM to encode a motion context. Internally, the TFM first employs a Feature Channel Gating (FCG) mechanism to explicitly evaluate the informational value of each feature channel. Specifically, the FCG utilizes global average pooling to aggregate spatial information and capture global channel statistics. These statistics are then used to generate a dynamic weighting vector that recalibrates the channel responses. By applying these learned weights, the FCG explicitly amplifies salient target features and suppresses redundant background noise induced by continuous ego-motion. The gating process yields a refined intermediate feature F_t , which is formulated as:

$$F_t = \sigma(\mathbf{W}_2 \cdot \text{ReLU}(\mathbf{W}_1 \cdot \text{GAP}(F_{ext}))) \otimes F_{ext}, \quad (2)$$

where F_{ext} represents the features from the frame feature extractor, $\text{GAP}(\cdot)$ denotes global average pooling, $\sigma(\cdot)$ is the sigmoid activation function, \mathbf{W}_1 and \mathbf{W}_2 are learnable weight matrices, and \otimes represents channel-wise multiplication.

The enhanced feature F_t is subsequently processed by a Motion Context Encoder to capture cross-slice kinematics, yielding the Temporal Context Vector (TCV). This vector is concatenated with the appearance features from the spatial anchor frame. This architectural design enables the network to implicitly learn spatial alignment and spatio-temporal correlations between consecutive slices, bypassing the need for computationally prohibitive optical flow estimation or precise IMU-based ego-motion compensation.

3) *Scale-Aware Loss*: The YOLOX framework originally employs standard IoU loss, but this metric is suboptimal for targets with extreme scale variations. Specifically, the changing distance between the target drone and the spinning camera induces significant scale changes in MSR. To prevent regression degradation for distant, small-scale targets, we replace this baseline with Efficient IoU (EIoU) loss [30]:

$$\mathcal{L}_{EIoU} = \mathcal{L}_{IoU} + \frac{\rho^2(b, b_{gt})}{c^2} + \frac{\rho^2(w, w_{gt})}{w_c^2} + \frac{\rho^2(h, h_{gt})}{h_c^2}, \quad (3)$$

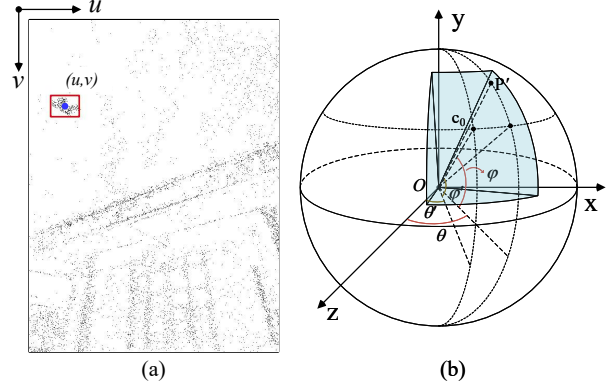


Fig. 5: *Coordinate systems and bearing estimation*. (a) Image plane: Detection result with a red bounding box marking the drone and a dot indicating its centroid. (b) Spinning platform system: The detected centroid is projected into the 3D coordinate system (origin: camera optical center; y-axis: rotation axis; z-axis: zero-direction). This projection enables bearing calculation.

where $\rho(\cdot)$ represents the Euclidean distance, c is the diagonal length of the smallest enclosing box covering the predicted box b and the ground truth box b_{gt} , while w_c and h_c denote its width and height, respectively. By independently regularizing the width and height to provide direct gradients, EIoU ensures consistent localization accuracy and robust bounding box regression across a wide range of operational distances, from close-range encounters to long-distance tracking.

4) *Bearing Estimation*: After obtaining the detection results from the network, we compute the bearing to the drone relative to our system using a projection method inspired by CMax-SLAM [31]. As illustrated in Fig. 5 (a), the drone centroid (u, v) is defined as the center of the detection bounding box.

The normalized bearing vector in image coordinates is

$$\mathbf{X}_P = \mathbf{K}^{-1}(u, v, 1)^\top, \quad (4)$$

where \mathbf{K} is the camera intrinsic matrix. This vector is then transformed into the spinning platform’s coordinate system using the rotation:

$$\mathbf{X}_{P'} = \mathbf{R}(\theta')\mathbf{R}(\phi')\mathbf{X}_P, \quad (5)$$

where $\mathbf{R}(\theta')$ and $\mathbf{R}(\phi')$ represent the rotation matrices for the spinning platform’s motion and the camera’s fixed installation tilt, respectively. The instantaneous angle of the spinning platform is given by $\theta' = (t - t_0)\omega$, where t_0 is the reference time when the platform passes the zero direction, t is the detection timestamp, and ω is the angular velocity.

Finally, the rotated point $\mathbf{X}_{P'} = (X_{P'}, Y_{P'}, Z_{P'})^\top$ (see Fig. 5(b)) is transformed into the spherical coordinate system, with its angular representation given by

$$\phi = \arcsin \frac{Y_{P'}}{\sqrt{X_{P'}^2 + Y_{P'}^2 + Z_{P'}^2}}, \quad \theta = \arctan \frac{X_{P'}}{Z_{P'}}, \quad (6)$$

where ϕ and θ represent the estimated bearing of the drone in the spinning platform coordinate system.

IV. EXPERIMENTS

This section presents a comprehensive evaluation of the proposed system to validate its effectiveness and efficiency. Our evaluation is structured as follows: We first introduce the experimental details (Sec. IV-A). Then, we analyze the performance of the network in lighting conditions and present an ablation study (Sec. IV-B). Finally, we demonstrate the real-world performance through outdoor onboard tests (Sec. IV-C).

A. Experimental Details

1) *Training Setup*: The network is trained on a server equipped with an NVIDIA RTX A6000 GPU (48 GB VRAM), a 30-core Intel Xeon Platinum 8336C CPU, and 60 GB of RAM. A batch size of 64 is used with the Adam optimizer at an initial learning rate of 0.0001. The loss function combines EIoU loss, L1 loss, classification loss, and binary cross-entropy loss. All layers are randomly initialized from scratch.

2) *Experimental Setup*: The proposed system is mounted on a Unitree Go2-W quadruped robot to enable autonomous locomotion. Onboard computation is handled by an NVIDIA Jetson Orin NX (16 GB LPDDR5) configured for maximum performance (25 W mode). The model is optimized and converted to TensorRT with FP16 precision. A DJI Mini 4K serves as the detection target.

3) *Ground Truth Acquisition*: Ground truth trajectories and poses are obtained by fusing data from GNSS receivers on both our device and the drone, together with a MID-360 LiDAR integrated with the quadruped robot. The poses of our device are further refined using FAST-LIO [32], while trajectory fitting and GPS-LiDAR alignment generate the carrier’s trajectory and pose at each time instant. To minimize timing errors, our system adopts strict time synchronization, with a particular design worth highlighting: an STM32 microcontroller processes both the PPS signal from the GNSS module and the trigger from the photoelectric switch before forwarding them to the camera. As the camera accepts only a single external trigger, the two signals are configured at different frequencies to ensure reliable separation.

4) *Baseline Considerations*: Current SOTA event-based methods rely on specific assumptions, such as static backgrounds [8] or low-speed motion [19], to maintain stable representations. These priors are violated by the severe spatial misalignment in our spinning scenario, making these methods impractical on our data. Instead, our framework is explicitly designed for continuous high-dynamic ego-motion, leveraging the high temporal resolution nature of events without relying on stable background priors. Consequently, we employ our spatial-only backbone as the primary baseline to rigorously isolate the TFM’s contribution under high-dynamic conditions.



Fig. 6: Illustration of detection results under varying lighting conditions. Top: High-glare scenario with the sun directly within the camera’s FoV during the afternoon. Bottom: Low-light scenario after sunset.

TABLE II: Evaluation under varying lighting conditions [%]. Minimum Detectable Size (MDS) denotes the smallest target width identifiable by the network under the corresponding scenario. In high-glare scenarios, we deem that size-based comparison is not particularly meaningful; therefore, this aspect is not included in the experimental evaluation.

Illumination	AP	AP ₇₅	AR ₁₀₀	MDS [pixels]
Standard	62.19	69.70	67.12	14
Low	59.30	63.80	62.60	17
High	55.80	58.20	60.20	-

5) *Evaluation Metric*: The drone’s bearing in the world coordinate system is represented as a unit vector derived from its spherical coordinates (θ, ϕ) , where θ and ϕ denote the azimuth and elevation angles, respectively. To quantify the estimation accuracy, we compute the angular error γ between the estimated bearing vector \vec{v}_{est} and the ground truth vector \vec{v}_{GT} . This error is defined as the true 3D angle between the two vectors:

$$\gamma = \arccos(\vec{v}_{\text{est}} \cdot \vec{v}_{\text{GT}}). \quad (7)$$

This metric accurately measures the shortest angular distance between the two directions in 3D space.

For the detection performance, for the performance of the network, we adopt Average Precision (AP), AP at 75% IoU (AP₇₅), and Average Recall at 100 detections (AR₁₀₀) as the main evaluation metrics for recognition results.

B. Detection Performance

In this section, we evaluate the performance of the network, beginning with an assessment of key detection metrics under challenging illumination conditions, followed by an ablation study to validate the contribution of the proposed module.

1) *Performance Under Varying Lighting Conditions*: To validate the robustness of the proposed network in outdoor conditions, we evaluate its performance under three selected

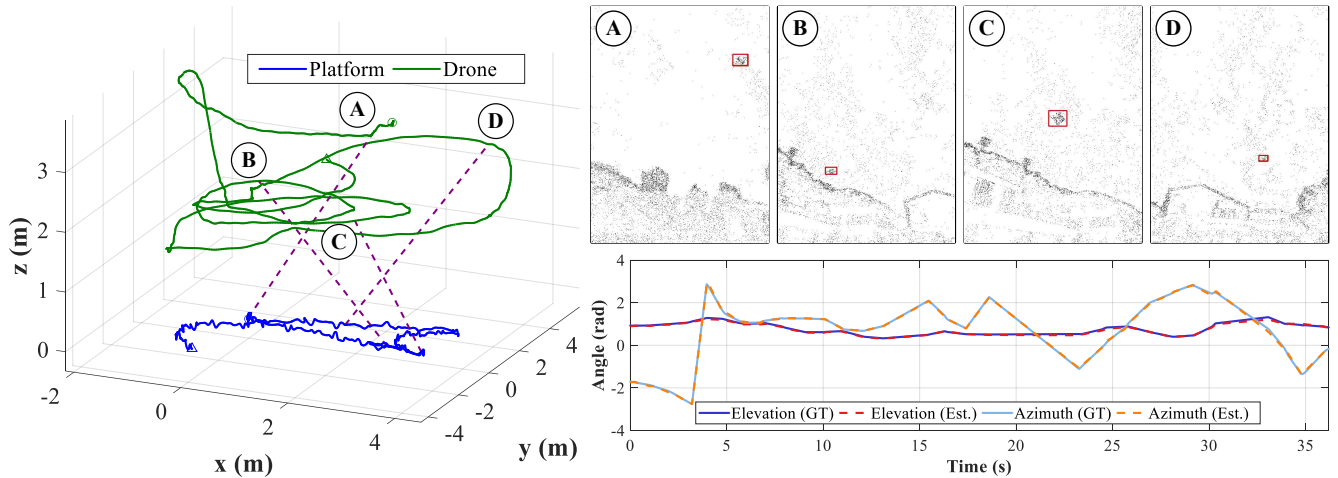


Fig. 7: *Illustration of the detection results.* Left: Trajectories of the carrier and drone, with four representative time instants marked by circled letters and connected by purple dashed lines. Top right: Corresponding camera images showing the detection results, where drone detection results are highlighted. Bottom right: Comparison of the estimated angles (Est.) with the ground truth (GT), with GPS data interpolated using cubic splines to obtain the drone’s position at the exact detection moments.

TABLE III: *Ablation study of temporal fusion.* Up or down arrows (\uparrow or \downarrow) indicate whether a higher or lower value is better. Network parameters (Params) represent the total number of learnable weights in the network.

Metric	w/o Temporal Fusion	w/ Temporal Fusion
AP \uparrow [%]	62.19	64.92 (+2.73)
AP $_{75}$ \uparrow [%]	69.70	72.80 (+3.10)
AR $_{100}$ \uparrow [%]	67.12	69.87 (+2.75)
AP $_S$ \uparrow [%]	56.30	59.90 (+3.60)
Params \downarrow [M]	8.94	9.53

lighting scenarios: standard illumination, low-light conditions, and high-glare conditions with the sun within the camera’s FoV.

Fig. 6 provides a visualization of these lighting conditions. Under high illumination (top row), solar over-exposure highlights clouds while suppressing intensity changes from the drone and structures, causing the drone to appear washed out and blend into the background. Under low light (bottom row), reduced contrast and lack of self-emission make it difficult to detect the drone without propeller motion; lower event counts introduce more noise, further complicating detection. Quantitative results (Tab. II) show strong performance in standard lighting. Under strong illumination, metrics decline due to feature loss from overexposure, though baseline detection remains feasible. In low light, accuracy is maintained with only slight degradation.

In summary, these experiments confirm that our event-based detection system is not only effective under ideal conditions but also exhibits superior robustness to extreme illumination variations that typically hinder frame-based approaches. This capability is a direct result of the inherent properties of the event sensor, combined with our designed processing pipeline, underscoring the system’s suitability for

TABLE IV: Evaluation on self-recorded sequences using angular error [$^\circ$].

Sequences	Mean error [$^\circ$]	Median error [$^\circ$]	Max error [$^\circ$]
<i>static_1</i>	2.063	2.096	3.103
<i>static_2</i>	1.772	1.764	2.611
<i>static_3</i>	1.736	1.715	2.835
<i>static_4</i>	1.858	1.848	3.144
<i>moving_1</i>	2.004	1.857	4.340
<i>moving_2</i>	1.927	1.921	4.308

real-world deployment where lighting cannot be controlled.

2) *Ablation Study:* In this section, we validate the impact of the Temporal Fusion Module, the key contribution of the system, on the performance of the network. The results of the ablation study are summarized in Tab. III. Consistent improvements are observed across all major detection metrics when the Temporal Fusion Module is incorporated, notably in AP at multiple thresholds and recall rates. The parameter count increases slightly. However, subsequent onboard experiments further confirm that this modest rise in parameter count does not compromise the real-time performance of the system, demonstrating that the proposed module enhances representational capacity efficiently without incurring significant computational overhead.

C. Outdoor Experiment

To assess the practicality of our system, we conduct six outdoor experiments, comprising four sequences under stationary conditions and two under carrier motion. The evaluation results are presented in Tab. IV. The stationary sequences yield stable and concentrated error distributions, whereas the moving sequences exhibit more dispersed errors with larger peaks, reflecting the impact of dynamic disturbances. It should also be noted that the ground truth data in the dynamic experiments rely on the Fast-LIO algorithm,

TABLE V: Computational performance on different platforms [Time: ms].

Node	Function	Laptop	Jetson NX
Pre-processing	Data processing	0.969	1.938
	Image generation	10.841	30.514
Detection	Input construction	3.762	5.223
	Inference	11.440	20.425
	Bearing estimation	0.0475	0.0823
	Others	15.249	18.467
	Subtotal	27.335	44.938

which may degrade under rapid motion; hence, the reported errors may stem from both system inaccuracies and reference uncertainties.

The results indicate that azimuth (θ) estimation remains accurate, whereas elevation (ϕ) exhibits larger deviations. This is likely because locomotion-induced jitter of the quadruped robot has a greater impact on pose interpolation accuracy in the vertical direction. Quantitatively, sequence *moving_1* yields a mean error of about 2° , with deviations occasionally exceeding 4° , confirming reliable performance under motion-induced fluctuations. Despite the increased error under motion, the system maintains functional performance and provides usable bearing estimates even under the challenging conditions of quadruped locomotion. We visualize the bearing estimation results on a moving carrier in Fig. 7. Despite the severe ego-motion, the estimates closely align with the ground truth, demonstrating the system’s capacity to maintain robust and reliable target localization

D. Computational Efficiency

To assess the computational performance of our algorithm, we conduct experiments on the *moving_1* sequence using two different platforms: a laptop (AMD Ryzen R7 5800H, RTX 3060 GPU) and an embedded platform (NVIDIA Jetson Orin NX). Table V reports the average runtime of each processing module, providing a detailed breakdown of the computational resource allocation on different hardware.

Our system, implemented in C++, consists of two processes. The pre-processing node converts the events into image, with the entire process executed on the CPU. The computational bottleneck is the detection node, which involves *input construction*, *inference*, and *bearing estimation*. The Inference part is accelerated with TensorRT, while the other components are processed on the CPU. The “Others” category primarily includes the time required for transferring event representations from the CPU to the GPU. The subtotal runtime of the detection node confirms that our system can operate stably in real time at 30 Hz on the desktop platform and approximately 22 Hz on the embedded platform.

V. CONCLUSION

We present ODD-SEC, a system that enables 360° horizontal perception on moving carriers to detect drones and estimate their bearing in real time. By mounting an event

camera on a spinning platform, our system significantly expands the FoV, overcoming the inherent FoV limitations of traditional event camera setups. Correspondingly, we propose a novel event representation and a lightweight neural network, which allow drone detection without motion compensation and further realize bearing estimation, even when the carrier is in motion. Extensive outdoor experiments under both stationary and dynamic conditions validate the accuracy and robustness of our approach, yielding a mean angular error of only 1.91° , and demonstrate real-time performance at 22 Hz on Jetson Orin NX. Future work will explore trajectory prediction, autonomous navigation and mapping, and closed-loop deployment in complex environments, along with code release to support further research.

REFERENCES

- [1] A.-I. Siean, R.-D. Vatavu, and J. Vanderdonck, “Taking that perfect aerial photo: A synopsis of interactions for drone-based aerial photography and video,” in *Proceedings of the 2021 ACM International Conference on Interactive Media Experiences*, 2021, pp. 275–279.
- [2] F. Hong, G. Wu, Q. Luo, H. Liu, X. Fang, and W. Pedrycz, “Logistics in the sky: A two-phase optimization approach for the drone package pickup and delivery system,” *IEEE Transactions on Intelligent Transportation Systems*, vol. 24, no. 9, pp. 9175–9190, 2023.
- [3] V. Sowmya, A. S. Janani, S. M. Hussain, A. Aashica, and S. Arvindh, “Creating a resilient solution: Innovating an emergency response drone for natural disasters,” in *2024 10th International Conference on Communication and Signal Processing (ICCSP)*. IEEE, 2024, pp. 344–348.
- [4] H. Rahmani and G. R. Weckman, “Working under the shadow of drones: investigating occupational safety hazards among commercial drone pilots,” *IIEE Transactions on Occupational Ergonomics and Human Factors*, vol. 12, no. 1-2, pp. 55–67, 2024.
- [5] G. Gallego, T. Delbrück, G. Orchard, C. Bartolozzi, B. Taba, A. Censi, S. Leutenegger, A. J. Davison, J. Conradt, K. Daniilidis, et al., “Event-based vision: A survey,” *IEEE transactions on pattern analysis and machine intelligence*, vol. 44, no. 1, pp. 154–180, 2020.
- [6] Y. Zhou, G. Gallego, X. Lu, S. Liu, and S. Shen, “Event-based motion segmentation with spatio-temporal graph cuts,” *IEEE transactions on neural networks and learning systems*, vol. 34, no. 8, pp. 4868–4880, 2021.
- [7] Z. Wang, T. Molloy, P. Van Goor, and R. Mahony, “Asynchronous blob tracker for event cameras,” *IEEE Transactions on Robotics*, 2024.
- [8] D. R. Da Costa, M. Robic, P. Vasseur, and F. Morbidi, “A new stereo fisheye event camera for fast drone detection and tracking,” in *IEEE International Conference on Robotics and Automation*, 2025.
- [9] X. Luo, M. Yao, Y. Chou, B. Xu, and G. Li, “Integer-valued training and spike-driven inference spiking neural network for high-performance and energy-efficient object detection,” in *Eur. Conf. Comput. Vis. (ECCV)*, 2024.
- [10] S. Sanyal, R. K. Manna, and K. Roy, “Ev-planner: Energy-efficient robot navigation via event-based physics-guided neuromorphic planner,” *IEEE Robotics and Automation Letters*, vol. 9, no. 3, pp. 2080–2087, 2024.
- [11] Q. Su, Y. Chou, Y. Hu, J. Li, S. Mei, Z. Zhang, and G. Li, “Deep directly-trained spiking neural networks for object detection,” in *Int. Conf. Comput. Vis. (ICCV)*, 2023, pp. 6555–6565.
- [12] S. Schaefer, D. Gehrig, and D. Scaramuzza, “Aegnn: Asynchronous event-based graph neural networks,” in *Proceedings of the IEEE/CVF Conference on Computer Vision and Pattern Recognition (CVPR)*, June 2022, pp. 12 371–12 381.
- [13] Y. L. Z. Y. Z. C. B. Zhang, “Graph-based asynchronous event processing for rapid object recognition,” in *Int. Conf. Comput. Vis. (ICCV)*, 2021, pp. 934–943.
- [14] Y. Peng, Y. Zhang, Z. Xiong, X. Sun, and F. Wu, “Get: Group event transformer for event-based vision,” in *Proceedings of the IEEE/CVF International Conference on Computer Vision*, 2023, pp. 6038–6048.
- [15] N. Zubić, D. Gehrig, M. Gehrig, and D. Scaramuzza, “From chaos comes order: Ordering event representations for object recognition and detection,” in *Proceedings of the IEEE/CVF International Conference on Computer Vision*, 2023, pp. 12 846–12 856.

- [16] M. Gehrig and D. Scaramuzza, "Recurrent vision transformers for object detection with event cameras," in *Proceedings of the IEEE/CVF conference on computer vision and pattern recognition*, 2023, pp. 13 884–13 893.
- [17] D. Li, Y. Tian, and J. Li, "Sodformer: Streaming object detection with transformer using events and frames," *IEEE Transactions on Pattern Analysis and Machine Intelligence*, vol. 45, no. 11, pp. 14 020–14 037, 2023.
- [18] A. Tomy, A. Paigwar, K. S. Mann, A. Renzaglia, and C. Laugier, "Fusing event-based and rgb camera for robust object detection in adverse conditions," in *2022 International Conference on Robotics and Automation (ICRA)*, 2022, pp. 933–939.
- [19] Y. Chen and L. Wang, "emoe-tracker: Environmental moe-based transformer for robust event-guided object tracking," *IEEE Robotics and Automation Letters*, vol. 10, no. 2, pp. 1393–1400, 2025.
- [20] G. Magrini, F. Becattini, P. Pala, A. Del Bimbo, and A. Porta, "Neuromorphic drone detection: An event-rgb multimodal approach," in *Computer Vision – ECCV 2024 Workshops*, A. Del Bue, C. Canton, J. Pont-Tuset, and T. Tommasi, Eds. Cham: Springer Nature Switzerland, 2025, pp. 259–275.
- [21] N. Sanket, C. Singh, C. Parameshwara, C. Fermüller, G. de Croon, and Y. Aloimonos, "Evpropnet: Detecting drones by finding propellers for mid-air landing and following," in *Robotics Science and Systems*, 2021.
- [22] Y. Zhang, Z. Ning, X. Zhang, S. Guo, P. Liu, and S. Zhao, "Evdet-mav: Generalized mav detection from moving event cameras," *IEEE Robotics and Automation Letters*, vol. 10, no. 8, pp. 8236–8243, 2025.
- [23] P. K. Jaisawal, S. Papakonstantinou, and V. Gollnick, "Airfisheye dataset: A multi-model fisheye dataset for uav applications," in *2024 IEEE International Conference on Robotics and Automation (ICRA)*. IEEE, 2024, pp. 11 818–11 824.
- [24] Z. Wang, K. Yang, H. Shi, P. Li, F. Gao, and K. Wang, "Lf-vio: A visual-inertial-odometry framework for large field-of-view cameras with negative plane," in *2022 IEEE/RSJ International Conference on Intelligent Robots and Systems (IROS)*. IEEE, 2022, pp. 4423–4430.
- [25] A. Saxena, H. Pandya, G. Kumar, A. Gaud, and K. M. Krishna, "Exploring convolutional networks for end-to-end visual servoing," in *2017 IEEE International Conference on Robotics and Automation (ICRA)*. IEEE, 2017, pp. 3817–3823.
- [26] Q. Bateux, E. Marchand, J. Leitner, F. Chaumette, and P. Corke, "Training deep neural networks for visual servoing," in *2018 IEEE international conference on robotics and automation (ICRA)*. IEEE, 2018, pp. 3307–3314.
- [27] S. Schraml, A. N. Belbachir, and H. Bischof, "An event-driven stereo system for real-time 3-d 360 panoramic vision," *IEEE Transactions on Industrial Electronics*, vol. 63, no. 1, pp. 418–428, 2015.
- [28] Z. Ge, S. Liu, F. Wang, Z. Li, and J. Sun, "Yolox: Exceeding yolo series in 2021," *arXiv preprint arXiv:2107.08430*, 2021.
- [29] X. Lagorce, G. Orchard, F. Galluppi, B. E. Shi, and R. B. Benosman, "Hots: A hierarchy of event-based time-surfaces for pattern recognition," *IEEE Transactions on Pattern Analysis and Machine Intelligence*, vol. 39, no. 7, pp. 1346–1359, 2017.
- [30] Y.-F. Zhang, W. Ren, Z. Zhang, Z. Jia, L. Wang, and T. Tan, "Focal and efficient iou loss for accurate bounding box regression," *Neurocomputing*, vol. 506, pp. 146–157, 2022.
- [31] S. Guo and G. Gallego, "Cmax-slam: Event-based rotational-motion bundle adjustment and slam system using contrast maximization," *IEEE Transactions on Robotics*, vol. 40, pp. 2442–2461, 2024.
- [32] W. Xu and F. Zhang, "Fast-lio: A fast, robust lidar-inertial odometry package by tightly-coupled iterated kalman filter," *IEEE Robotics and Automation Letters*, vol. 6, no. 2, pp. 3317–3324, 2021.